IEEE Sensors Council IEEE SENSORS JOURNAL, VOL. 23, NO. 3, 1 FEBRUARY 2023

A Lightweight, Zero-Power Intermodulation Sensor Based on the Graphene Oscillator

Minye Yang, Zhilu Ye, Chia-Heng Sun, Liang Zhu, Mehdi Hajizadegan, *Senior Member, IEEE*, and Pai-Yen Chen, *Senior Member, IEEE*

***Abstract*—Wireless sensor networks (WSNs) require a massive number of sensor nodes for data collection and storage, for which the power management and area efficiency of battery-powered sensors may be an issue. In this article, we propose and numerically study a fully passive and lightweight intermodulation sensor based on the reconfigurable graphene field-effect transistors (GFETs) oscillator and passive frequency mixer. The output frequency of the self-powered GFET-based oscillator can be sensitive to the surface doping effect caused by charged surface absorbates, reactive gases, contaminations, or aqueous solutions. In the intermodulation sensor, the low-frequency signals generated by GFET oscillator are mixed with the incident radio frequency (RF) waves, forming the retransmitted and the RF intermodulation signals. Since the intermodulation products do not mess up with the reception signal, the unwanted clutters, self-jamming, and interferences can be effectively suppressed. Our results show that the output frequency of the GFET oscillator can sensitively respond to charged molecules, and such information can be encoded in the backscatter intermodulation signal. We believe that our GFET-based intermodulation sensor may be beneficial for a variety of the Internet of Things (IoTs), remote sensing, and environment monitoring applications.**

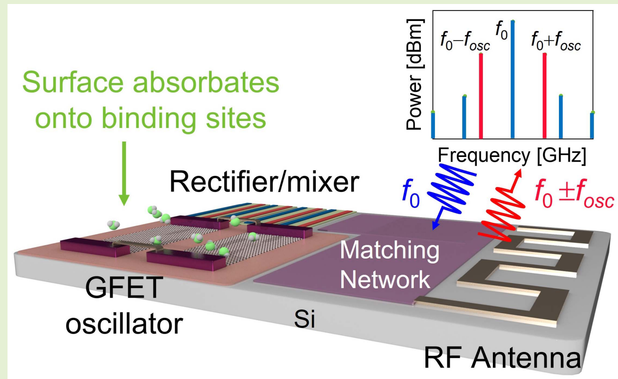

***Index Terms*—Clutters, fully passive wireless sensor, graphene field-effect transistor (GFET), intermodulation, radio frequency (RF) sensor, self-jamming.**

I. Introduction

COMPACT and energy-efficient wireless sensors capable of continuously monitoring the environmental parameters, such as temperature [1], [2], pressure [3], [4], light intensity [5], humidity [6], and air quality [7], are essential in wireless sensor networks (WSNs) [8], [9], [10] and the Internet-of-Things (IoTs) [11], [12] applications. The ever-increasing demand for these countless sensors has brought several challenges, such as how to design power- and area-efficient sensors and how to operate in rich-scattering indoor and urban environments. To resolve these challenges, various types of passive wireless sensors have been proposed, such as backscatter radio frequency identification (RFID) [13], [14], surface acoustic wave (SAW)-based RFID [15], chipless resonant tags [16], [17], [18], near-field *LC* sensors [19], [20], and harmonic transponder sensors [21], [22], [23], [24]. These passive wireless sensors are expected to reduce the maintenance cost and power consumption of WSNs, while increasing the lifetime, when compared with active battery-powered sensors [25], [26]. However, these devices more or less face one of the aforementioned problems. For instance, a miniature sensor is usually integrated with the passive backscatter RFID to wirelessly transmit the sensor information in the form of amplitude modulation (AM) or frequency modulation (FM). However, clutters, self-jamming, and electromagnetic interferences existing in noisy environments may affect the sensing accuracy and reliability and also shorten the readout distances of the RFID systems [27]. Although wireless sensors based on the harmonic transponders can effectively suppress interferences [28], [29], [30], they lack spectral efficiency (due to the use of harmonics) and could increase the design complexity and area of readers and sensors.

The concept of clutter suppression using intermodulation responses was first proposed for radar systems and then extended to wireless sensing, such as readout of

Manuscript received 19 December 2021; revised 9 August 2022; accepted 5 December 2022. Date of publication 13 December 2022; date of current version 31 January 2023. This work was supported by the National Science Foundation Electrical, Communications and Cyber Systems (ECCS) under Grant 1914420. The associate editor coordinating the review of this article and approving it for publication was Prof. Mehdi Javanmard. *(Corresponding author: Pai-Yen Chen.)*

Minye Yang, Zhilu Ye, Chia-Heng Sun, Mehdi Hajizadegan, and Pai-Yen Chen are with the Department of Electrical and Computer Engineering, University of Illinois at Chicago, Chicago, IL 60607 USA (e-mail: pychen@uic.edu).

Liang Zhu is with Maxtena Inc., Rockville, MD 20855 USA.

Digital Object Identifier 10.1109/JSEN.2022.3227891

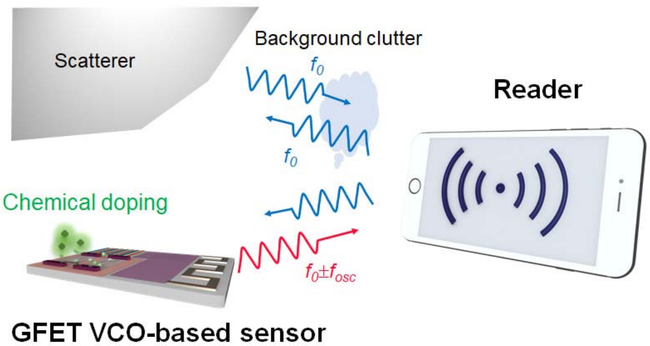

Fig. 1. Schematic of sensing setup of GFET intermodulation sensor in a cluttered environment. The GFET sensor can sensitively respond to the chemical doping (e.g., surface absorbates or charged molecules) by a retransmitted and frequency-reconfigurable intermodulation signal, which does not mess with the incident RF signal.

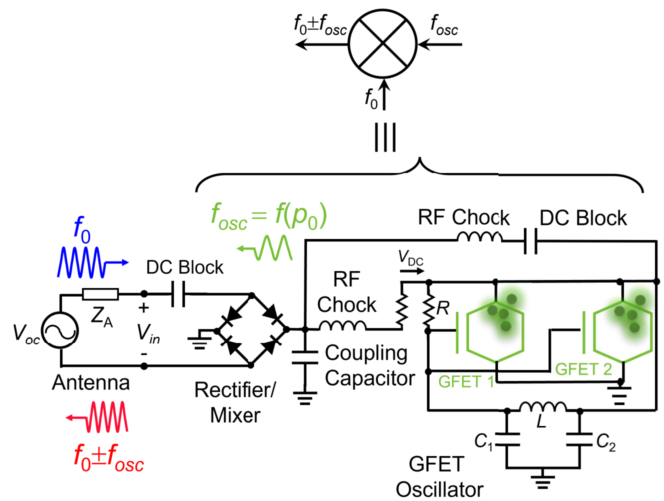

Fig. 2. Circuit diagram of GFET intermodulation sensor composed of an RF antenna, a full-bridge diode rectifier/mixer, and a nonbuffered inverter-based oscillator formed by two GFETs.

micromachined wireless sensors that have a very small footprint [31], [32]. The main advantage of intermodulation-based sensors over harmonic-based sensors is that the frequency offset is much smaller, which not only facilitates circuit and antenna design to reduce area occupation but also improves the spectral efficiency to meet frequency compliance. Moreover, intermodulation sensors can still effectively suppress interferences as their harmonic counterparts. Despite of these advantages, the intermodulation sensors in [33] and [34] generally require at least two separate modules: a local oscillator implemented by nonlinear elements (e.g., MOSFETs, diodes, etc.) and a sensing module, such as a commercial capacitive sensor [33], which will increase the design complexity, device area, and cost due to packaging and integration.

To overcome this challenge, we herein propose a lightweight graphene field-effect transistor (GFET)-based intermodulation sensor for the detection of charged molecules in the air or aqueous solutions, as shown in Fig. 1. Graphene has been intensively studied owing to its excellent electronic, mechanical, and thermal properties [35], [36], [37], [38]. The linear and gapless energy dispersion at Dirac point, resulting in a relatively low density of states, make the graphene devices very sensitive to electrostatic or chemical doping environments [39], [40], [41]. To date, researchers have proposed a variety of applications of such Dirac material, ranging from ultrasensitive biosensors [23], [42], protein sensors [43], gas sensors [44], deoxyribonucleic acid (DNA) and aptamer sensors [45], [46], high-frequency field-effect transistors (FETs) [47], and tunable plasmonic devices [48], [49], [50]. Among those lines, the GFETs have gained their great success due to the remarkable ambipolar transfer ($I_{DS} \sim V_{GS}$) characteristics. A zero drain-to-source current may be achieved when the applied gate voltage equals to the Dirac voltage [51], which is also referred to as the charge neutrality point (V_{cnp}). According to the charge conservation on the graphene channel, any charged carrier absorbed on the graphene surface may lead to the shift of V_{cnp}. In addition, the mobility of carriers in the graphene layer may respond to the variation of charged carrier density, varying dynamically the drain-to-source current.

Fig. 2 shows the proposed intermodulation sensor, which comprises a radio frequency (RF) antenna, a rectifier/mixer, and a GFET-based oscillator (which simultaneously serves as the frequency synthesizer and the sensing element). This intermodulation sensor receives the incident radio signal at fundamental frequency f_0 (2.4 GHz) and transmits the modulated signal at the intermodulation frequency $f_0 \pm f_{osc}$, where f_{osc} (a few megahertz) is the output frequency of the GFET oscillator. Due to the orthogonality between frequencies f_0 and $f_0 \pm f_{osc}$, clutter and interference problems found in traditional backscatter RFID sensor systems can be resolved [13], [14], [15]. Since $f_{osc} \ll f_0$, a single RF antenna can be used to receive the interrogation RF signal and transmit the intermodulation signal. The diode rectifier shown in Fig. 2 can convert the RF energy into dc electricity to power up the oscillator and also serve as the nonlinear element to mix the received RF signal with the local oscillator signal to generate the intermodulation signal. When the graphene channel in the back-gate GFET is exposed to (bio)chemical agents, molecules, or reactive gases, the surface doping effect could shift the output frequency of local oscillator f_{osc}, thereby encoding the sensor information in the FM results. Compared to current harmonic and intermodulation sensors, which are generally bulky and require an additional power source (e.g., battery or solar cell), the proposed self-powered GFET-based intermodulation sensor does not require any additional energy source. More interestingly, due to the unique chemically sensitive electronic properties of graphene, a back- or side-gate GFET can simultaneously function as both a frequency synthesizer and a sensor, making the entire system compact and lightweight.

II. Results and Discussion

A. Characteristics of GFET

Fig. 3(a) illustrates the back-gate GFET studied in this article, which has a surface functionalized graphene channel with receptors to selectively capture the (bio)chemical agents of interest. Here, we used a physics-based compact model to study the performance of GFET circuits. First, we measured the commercial GFETs (GFET S10 chip from Graphenea Inc.)

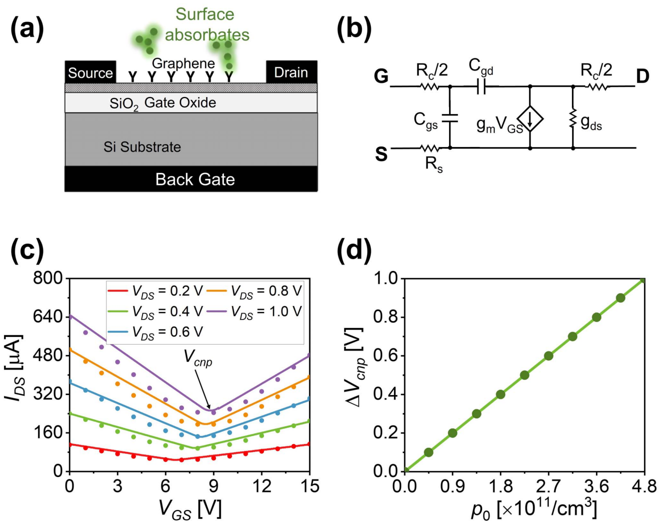

Fig. 3. (a) Schematic of a back-gate GFET and (b) its small-signal model. (c) Electrical characteristics of a back-gate GFET under different drain-to-source voltages ($V_{\mathrm{DS}} = 0.2$–1.0 V); here, solid lines and dots represent the simulation and experimental results, respectively. (d) Simulated V_{cnp} against the surface impurity density in the GFET channel.

to verify our compact model. The monolayer graphene channel was grown using the chemical vapor deposition (CVD) and then transferred onto the silicon on insulator (SOI) substrate with a 90-nm-thick SiO_2. Graphene channels were patterned using the oxygen plasma, and the source and drain electrodes (Ti/Au) were patterned using the electron beam evaporation. The important device parameters of the GFETs under test are listed in the following. The SiO_2 gate oxide has a thickness $t_{\mathrm{ox}} = 90$ nm and dielectric constant $\varepsilon_{\mathrm{ox}} = 4$. The length and the width of graphene channel are $L = 50$ μm and $W = 50$ μm, respectively.

The I–V characteristics of the GFET can be obtained from the drift-diffusion transport model, where the drain-to-source current is given by [52]

$$I_{\mathrm{DS}} = qW\,|Q_s(x)|\,\upsilon_{\mathrm{drift}}(x) = \frac{W}{L_{\mathrm{eff}}}\int_0^{V_{\mathrm{DS}}} \mu_{\mathrm{eff}}\,|Q_s|\,dV. \quad (1)$$

where q is the charge of a single electron, $L_{\mathrm{eff}} = L - \int_0^{V_{\mathrm{DS}}} 1/\nu_{\mathrm{sat}} dV$ is the effective channel length resulting from the saturation drift velocity of carriers ν_{drift}, which is assumed to be half of the Fermi velocity $\nu_F = 10^8$ cm/s, μ_{eff} denotes the effective carrier mobility, and V_{DS} represents the channel voltage drop across the graphene channel (see Appendix for explicit expressions of surface charge density Q_s and I_{DS}). The effective carrier mobility in (1) can be expressed as [53]

$$\mu_{\mathrm{eff}} = \frac{n\mu_n + n\mu_p + n_{\mathrm{pud}}(\mu_n + \mu_p)/2}{n + p + n_{\mathrm{pud}}}\left(\frac{m}{m + V_{\mathrm{ch}}^2}\right) \times \frac{1}{1 + (T/T_{\mathrm{ref}} - 1)^{\beta}} \quad (2)$$

where, according to the experimental measurements, $\mu_n = 1450$ cm^2/V $\cdot$ s, $\mu_p = 1650$ cm^2/V $\cdot$ s, $n_{\mathrm{pud}} = 1.65 \times 10^{12}$ cm^{-2}, $m = 1$ is an empirical fitting parameter, $T_{\mathrm{ref}} = 300$ K, and $\beta = 3$. It is known from (2) that the surface charge density may influence the carrier mobility and hence the output current of the GFET. Then, the transconductance and the drain conductance of the GFET can be, respectively, calculated as $g_m = dI_{\mathrm{DS}}/dV_{\mathrm{GS}}|_{V_{\mathrm{DS}}=\mathrm{const}}$ and $g_{\mathrm{ds}} = dI_{\mathrm{DS}}/dV_{\mathrm{DS}}|_{V_{\mathrm{GS}}=\mathrm{const}}$. Fig. 3(b) shows the small-signal model of the GFET in (a), where the contact resistance is assumed to be $R_c = 0.12$ Ω [54], [55]. The influence of charged impurities, such as surface absorbates and chemical dopants in the graphene channel, which perturb the GFET's electrical characteristics, can be obtained from the charge conservation relation given by

$$C_{\mathrm{ox}}(V_{\mathrm{GS}} - V_{\mathrm{cnp}} - V(x)) + Q_s = 0 \quad (3)$$

where C_{ox} is the gate oxide capacitance, $V(x) = (x/L)V_{\mathrm{DS}}$, and x signifies the position along the channel. The charge neutrality points V_{cnp} with the minimal drain-to-source current depend on the charged impurities absorbed onto the graphene surface. Therefore, upon receptor binding, the density of targeted (bio)chemical agents and molecules could p- or n-shift the V_{cnp}. Here, we assume a positively charged surface absorbates absorbed on the graphene channel, which triggers the p-doping effect and makes the V_{cnp} shift toward the positive direction ($\Delta V_{\mathrm{cnp}} > 0$). Fig. 3(c) shows the simulated I–V curves (solid lines) of the back-gate GFET under different drain-to-source voltages; here, the experimental results (dots) are also shown for making a comparison. It can be seen from Fig. 3(c) that increasing the modeling and measurement results is in a good agreement, except for the proximity of the charge neutral point (which could be ascribed to the existence of electron–hole puddles due to the fabrication flaws). Fig. 3(c) has fundamentally demonstrated that our physical compact model can predict the performance of GFET very well.

After validating the developed compact model of the back-gate GFET, we will use this compact model to design and simulate GFET-based voltage controlled oscillator (VCO). In order to achieve a higher drain-to-source current for the VCO operation, we assume $L = 7$ μm and $W = 2500$ μm, and the rest device parameters are the same as those used in Fig. 3(c). Fig. 3(d) shows the variation of V_{cnp} with respect to the density of charged absorbates on the graphene surface. It can be seen that when the density of positively charged dopants (p_0) increases from 0 to 4.8×10^{11}/cm^2, a strong p-shift of V_{cnp} can be obtained. This linear relationship between the p-shift of V_{cnp} and the surface impurity density can be written as: $qp_0 = C_{\mathrm{ox}}\Delta V_{\mathrm{cnp}}$. Both μ_{eff} and V_{cnp} are affected by (bio)chemical agents, gases, and molecules appearing on the graphene surface, altering the electrical characteristics of a back- or side-gate GFET. As a result, an oscillator built based on GFET can be chemically sensitive and has a reconfigurable output frequency. This is very different from traditional CMOS oscillator and will provide a lightweight and highly integrabtible solution for making wireless biomolecular sensors, gas and air-quality sensors, humidity sensors, and so on.

B. Design and Evaluation of GFET Intermodulation Sensor

Fig. 2 shows the design and circuit diagram of the proposed GFET intermodulation sensor, which consists of: 1) a full-bridge diode rectifier with a matching network; 2) a chemically

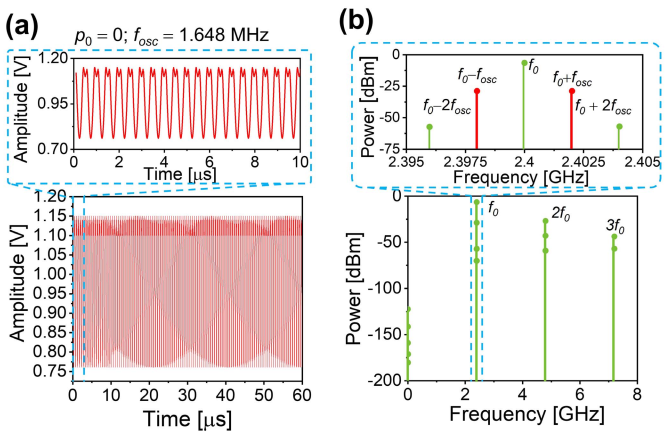

Fig. 4. (a) Time-domain waveform (transient response) of the GFET oscillator in the initial (undoped) status. The zoomed-in view window depicts the oscillation within first 10 μs. (b) Power spectrum of the output RF harmonic and intermodulation signals. The zoomed-in view window shows the intermodulation signals centered at the interrogation frequency (2.4 GHz). Here, the input power at the antenna terminal is 0 dBm.

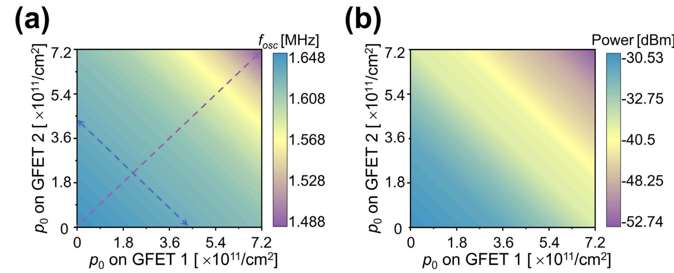

Fig. 5. Contours of (a) output oscillation frequency $f_{\rm osc}$ and (b) peak power at $f_{\rm osc}$ as a function of the surface impurity densities in GFET 1 and GFET 2 for the GFET oscillator shown in Fig. 2.

sensitive GFET-based oscillator; and 3) an RF antenna. Both the antenna and the rectifier are designed to operate near 2.4 GHz (f_0), which embraces the industry, science, and medical (ISM) band for many applications. The oscillator is designed based on the physics-based compact model ($L = 7\ \mu$m and $W = 2500\ \mu$m) and a nonbuffered inverter topology, which can operate under a low-power bias condition, with the important design parameters: $C_1 = 68$ pF, $C_2 = 210$ pF, $L = 180\ \mu$H, and $R = 10$ MΩ (see Fig. 2). For pristine graphene without doping (i.e., $V_{\rm cnp} = 0$ V), the output frequency of the GFET oscillator is $f_{\rm osc} \approx 1.648$ MHz. The resistor R in Fig. 2 acts as the feedback loop of the oscillator to stabilize the oscillation of the system. The full-bridge diode rectifier not only converts the RF energy to dc electricity for biasing oscillator but also acts as a frequency mixer to generate the intermodulation products. Based on the small-signal model in Section II-A, we performed numerical simulations using the Advanced Design System (ADS) to analyze the proposed GFET-based intermodulation sensor. The proposed GFET-based VCO can be manufactured using the standard lithography and interconnection processes for the integration circuits (ICs). The RF antenna can be integrated into a package along with the GFET chip.

We first assume that the rectifier receives 0-dBm RF power at 2.4 GHz from the input (feed point) of the antenna and the graphene channel is undoped. It can be seen from Fig. 4(a) that the GFET oscillator can successfully oscillate under the bias voltage produced by the rectifier, with the oscillation frequency $f_{\rm osc} \approx 1.648$ MHz. The transient response shown in Fig. 4(a) demonstrates a high-quality and stable oscillation at the time range of interest, especially the first 10 μs in the zoom-in window. This endows the intermodulation signal great readability and robustness. Here, we should note that since $f_{\rm osc} \ll f_0$, the intermodulation frequency $f_0 \pm f_{\rm osc}$ is still within the operating bandwidth of the antenna. Compared to the graphene harmonic sensor that requires two antennas or diplexer for handling the fundamental frequency input (f_0) and the second harmonic output ($2f_0$) [28], [56], [57], this GFET-based intermodulation sensor requires only one antenna and operates in the same spectrum (which is compatible to the frequency-hopping spread spectrum or FHSS system in 2.4-GHz band), thereby significantly reducing the sensor size and the design complexity of the system. In addition, when compared with current intermodulation sensors, this self-powered GFET oscillator can remove the power units (e.g., battery or solar cell) to squeeze the overall area occupation of the sensor. The calculated power levels of the intermodulation signals and their harmonics are presented in Fig. 4(b), where we notice from the zoom-in window that the intermodulation signals ($f_0 \pm f_{\rm osc}$) are close to -30 dBm with the carrier signal f_0 at -4-dBm power level, which is sufficiently high for the far-zone wireless sensing applications. The results depicted in Fig. 4 reveal that the intermodulation signal with sensing information ($f_0 \pm f_{\rm osc}$) embedded can propagate for a relatively long distance and be distinguishable from the background noise floor (~ -100 dBm).

Next, we will evaluate the sensitivity of the GFET intermodulation sensor. We consider that the two GFETs (GFET 1 and GFET 2) in the oscillator can absorb charged impurities independently. The oscillation frequencies and their power levels as functions of p_0 introduced to GFETs 1 and 2 are shown in Fig. 5(a) and (b), respectively. From Fig. 5(a) and (b), it can be seen that both the oscillation frequency and the power level are sensitive to the total surface charge density (i.e., concentration of surface absorbates) in the two GFETs. For instance, the sum of p_0 ($p_0 = 3.6 \times 10^{11}/\text{cm}^2$) applied onto the two GFETs is a constant along the blue dashed line, which corresponds to an unvaried oscillation frequency and the power modulation along this line. On the contrary, when the sum of p_0 disturbing the two GFETs increases along the purple dashed line from $p_0 = 0/\text{cm}^2$ to $p_0 = 7.2 \times 10^{11}/\text{cm}^2$, the frequency oscillation is varied from 1.648 to 1.488 MHz, while the power level of the oscillation is detuned from ~ -30 to ~ -52 dBm. Such a result demonstrates that the performances (i.e., oscillation frequency shift and power level modulation) of the GFET intermodulation sensor are determined by the total charged impurities in the two GFETs. Therefore, in the following analysis, we use p_0 to represent the total impurity density in the intermodulation sensor.

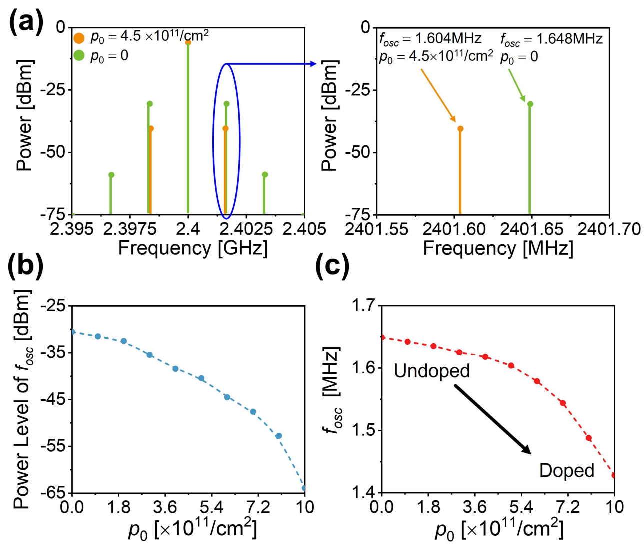

Fig. 6. (a) Output power spectra of the GFET intermodulation sensor before and after surface doping. The zoomed-in view window clearly shows that the frequency shift and the power modulation at $f_{\rm osc}$ are sensitive to binding of surface impurities on the graphene surface. (b) and (c) Modulation in power and output frequency of the GFET oscillator, in response to the increase in total surface charge density in the GFETs. Here, the input power at the antenna terminal is 0 dBm.

Fig. 6(a) shows the power spectra of the output intermodulation products at $p_0 = 0/\text{cm}^2$ and $p_0 = 4.5\times 10^{11}/\text{cm}^2$. The zoom-in window clearly shows that the intermodulation signal ($f_0 + f_{\rm osc}$) is shifted from 2401.648 to 2401.604 MHz, with the peak power being reduced from ~ -30 to ~ -40 dBm. Fig. 6(b) reports the dependency of the output power of intermodulation signal on the concentration of charged impurities p_0, showing that the conversion loss increases with increasing p_0 and a descent interrogation distance estimated by the Friis transmission formula. Fig. 6(c) reports the dependency of the output frequency of GFET oscillator on p_0, showing a shift from 1.648 to 1.488 MHz when the chemical dopant concentration increases. Such results suggest good sensitivity and resolvability. It is also worth mentioning that the proposed GFET-based intermodulation sensor may be integrated with a specific projection layer for maintaining uniform temperature, thereby stabilizing the sensor's performance. In this proof-of-concept demonstration, structural and material parameters of GFET were not yet optimized to achieve the maximum nonlinear frequency conversion efficiency. In a word, our work has demonstrated the feasibility of making a compact, lightweight, and fully passive GFET intermodulation sensor.

III. Conclusion

We have proposed a compact, lightweight, and fully passive intermodulation sensor based on a self-powered and reconfigurable GFET oscillator and a simple RF circuit. We have numerically analyzed the sensing performance of the intermodulation sensor, showing that the power and frequency of the backscattered intermodulation response are very sensitive to the amount of surface absorbates bound to the graphene surface (e.g., receptors or binding sites of surface-functionalized graphene). Our simulated results also show that, similar to harmonic sensors, the intermodulation sensor that receives and retransmits at different frequencies can be robust to clutters, self-jamming, and electromagnetic interferences. However, an intermodulation sensor has several advantages, such as reduced design complexity and device area, as well as much improved spectral efficiency, when compared with harmonic sensors. We expect that the GFET intermodulation sensor could pave the way for a wide variety of applications, including real-time detection of reactive gases, molecules, contaminations, and (bio)chemical agents, of essential importance for IoTs, WSNs, point-of-care testing, and wake-up radio systems.

Appendix

A. Transfer Characteristics of GFET

The drift-diffusion transport model suggests that the drain-to-source current takes the form of (1), where the mobile charge density Q_s in graphene is obtained as: $Q_s = q \times (p-n)$. Here, the electron and hole sheet densities (n and p) in graphene can be derived by integrating the density of states $D(E)$ weighted by the Fermi-Dirac distribution $f(E)$, which can be written as

$$n(E_F) = -\frac{2}{\pi}\left(\frac{K_B T}{\hbar v_F}\right)^2 Li_2\left[-e^{-qE_F/(K_B T)}\right]$$
$$p(E_F) = -\frac{2}{\pi}\left(\frac{K_B T}{\hbar v_F}\right)^2 Li_2\left[-e^{qE_F/(K_B T)}\right] \quad (4)$$

where the dilogarithm Li_2 is a special case of the polylogarithm $Li_n(\cdot)$ for $n = 2$, E_F is the Fermi level, $\hbar$ is the reduced Planck constant, v_F denotes the Fermi velocity ($v_F = 10^8$ cm/s), and K_B is the Boltzmann constant. By applying (4), the total mobile charge density can be expressed as

$$\begin{aligned} Q_s &= q \times (p-n) \\ &= q \times \left(\int_{-\infty}^{0} D(E)[1-f(E)]dE - \int_{0}^{\infty} D(E) f(E) dE\right) \\ &= q\frac{2}{\pi(\hbar v_F)^2}\int_0^\infty E\left[\frac{1}{e^{(E+E_F)/(K_B T)}+1} - \frac{1}{e^{(E-E_F)/(K_B T)}+1}\right] dE. \end{aligned} \quad (5)$$

The surface potential of the graphene channel $V_{\rm ch}$ is related to the Fermi level E_F, which is a function of the gate voltage $V_{\rm GS}$ given by [53], [58], [59], [60], [61], [62], [63], [64], [65], [66]

$$V_{\rm ch}(x) = E_F(x)/q = \frac{C_{\rm ox}}{C_{\rm ox} + 0.5C_q}(V_{\rm GS} - V_{\rm cnp} - V(x)) \quad (6)$$

where $C_{\rm ox} = \varepsilon_{\rm ox}/t_{\rm ox}$, $\varepsilon_{\rm ox}$ and $t_{\rm ox}$ are the dielectric constant and thickness of the oxidation layer, respectively, x is the position along the graphene channel, and C_q is the quantum capacitance having the expression of

$$C_q = \frac{\partial Q_s}{\partial V_{\rm ch}} = \frac{2q^2 K_B T}{\pi(\hbar v_F)^2}\ln\left[2\left(1+\cosh\frac{qV_{\rm ch}}{K_B T}\right)\right]. \quad (7)$$

By applying (4)–(7) to (1), an explicit expression of the drain-to-source current I_{ds} can be obtained as

$$I_{\mathrm{DS}} = \frac{\mu_{\mathrm{eff}} K}{2} \frac{W}{L_{\mathrm{eff}}} \left\{ \begin{array}{l} \left[-\frac{V_{\mathrm{ch}}^3(D)}{3} - \mathrm{sgn}(V_{\mathrm{ch}}(D)) \frac{K V_{\mathrm{ch}}^4(D)}{4C_{\mathrm{ox}}} \right] \\ - \left[-\frac{V_{\mathrm{ch}}^3(S)}{3} - \mathrm{sgn}(V_{\mathrm{ch}}(S)) \frac{K V_{\mathrm{ch}}^4(S)}{4C_{\mathrm{ox}}} \right] \end{array} \right\} \tag{8}$$

where $K = 2q^3/[(\pi \hbar \nu_F)^2]$, and $V_{\mathrm{ch}}(D)$ and $V_{\mathrm{ch}}(S)$ represent the surface potential of the channel at drain and source, respectively.

References

[1] Y. Wang, Y. Jia, Q. Chen, and Y. Wang, "A passive wireless temperature sensor for harsh environment applications," *Sensors*, vol. 8, pp. 7982–7995, Dec. 2008.

[2] S. Jeong, Z. Foo, Y. Lee, J.-Y. Sim, D. Blaauw, and D. Sylvester, "A fully-integrated 71 nW CMOS temperature sensor for low power wireless sensor nodes," *IEEE J. Solid-State Circuits*, vol. 49, no. 8, pp. 1682–1693, Aug. 2014.

[3] M. A. Fonseca, J. M. English, M. von Arx, and M. G. Allen, "Wireless micromachined ceramic pressure sensor for high-temperature applications," *J. Microelectromech. Syst.*, vol. 11, no. 4, pp. 337–343, Aug. 2002.

[4] J. Xiong et al., "Wireless LTCC-based capacitive pressure sensor for harsh environment," *Sens. Actuators A, Phys.*, vol. 197, pp. 30–37, Aug. 2013.

[5] H. Park, J. Burke, and M. B. Srivastava, "Design and implementation of a wireless sensor network for intelligent light control," in *Proc. 6th Int. Symp. Inf. Process. Sensor Netw.*, Cambridge, MA, USA, 2007, pp. 370–379.

[6] M. Borgese, F. A. Dicandia, F. Costa, S. Genovesi, and G. Manara, "An inkjet printed chipless RFID sensor for wireless humidity monitoring," *IEEE Sensors J.*, vol. 17, no. 15, pp. 4699–4707, Aug. 2017.

[7] J.-H. Liu et al., "Developed urban air quality monitoring system based on wireless sensor networks," in *Proc. 5th Int. Conf. Sens. Technol.*, Nov. 2011, pp. 549–554.

[8] D. Kandris, C. Nakas, D. Vomvas, and G. Koulouras, "Applications of wireless sensor networks: An up-to-date survey," *Appl. Syst. Innov.*, vol. 3, no. 1, p. 14, Feb. 2020.

[9] T. Cao-Hoang and C. N. Duy, "Environment monitoring system for agricultural application based on wireless sensor network," in *Proc. 7th Int. Conf. Inf. Sci. Technol. (ICIST)*, Apr. 2017, pp. 99–102.

[10] S. J. Ramson and D. J. Moni, "Applications of wireless sensor networks—A survey," in *Proc. Int. Conf. Innov. Elect., Electron., Instrum. Media Technol. (ICEEIMT)*, Coimbatore, India, 2017, pp. 325–329.

[11] K. A. M. Evans and S. A. A. Elmustafa, "Internet of Things applications, challenges and related future technologies," *World Sci. Newsr.*, vol. 2, no. 67, pp. 126–148, 2017.

[12] N. Khalil, M. R. Abid, D. Benhaddou, and M. Gerndt, "Wireless sensors networks for Internet of Things," in *Proc. IEEE 9th Int. Conf. Intell. Sensors, Sensor Netw. Inf. Process. (ISSNIP)*, Apr. 2014, pp. 1–6.

[13] D. P. Rose et al., "Adhesive RFID sensor patch for monitoring of sweat electrolytes," *IEEE Trans. Biomed. Eng.*, vol. 62, no. 6, pp. 1457–1465, Jun. 2015.

[14] A. M. J. Marindra and G. Y. Tian, "Chipless RFID sensor tag for metal crack detection and characterization," *IEEE Trans. Microw. Theory Techn.*, vol. 66, no. 5, pp. 2452–2462, May 2018.

[15] F. Li, D. Xiang, S. Chiang, B. R. Tittmann, and C. Searfass, "Wireless surface acoustic wave radio frequency identification (SAW-RFID) sensor system for temperature and strain measurements," in *Proc. IEEE Int. Ultrason. Symp.*, Oct. 2011, pp. 822–825.

[16] M. Sakhdari, M. Hajizadegan, Q. Zhong, D. N. Christodoulides, R. El-Ganainy, and P.-Y. Chen, "Experimental observation of PT symmetry breaking near divergent exceptional points," *Phys. Rev. Lett.*, vol. 123, no. 19, Nov. 2019, Art. no. 193901, doi: 10.1103/PhysRevLett.123.193901.

[17] P.-Y. Chen et al., "Generalized parity–time symmetry condition for enhanced sensor telemetry," *Nature Electron.*, vol. 1, no. 5, pp. 297–304, May 2018, doi: 10.1038/s41928-018-0072-6.

[18] Z. Ye et al., "A breathable, reusable, and zero-power smart face mask for wireless cough and mask-wearing monitoring," *ACS Nano*, vol. 16, no. 4, pp. 5874–5884, Apr. 2022, doi: 10.1021/acsnano.1c11041.

[19] Q.-A. Huang, L. Dong, and L.-F. Wang, "LC passive wireless sensors toward a wireless sensing platform: Status, prospects, and challenges," *J. Microelectromech. Syst.*, vol. 25, no. 5, pp. 822–841, Oct. 2016.

[20] M. Yang, Z. Ye, M. Farhat, and P.-Y. Chen, "Ultrarobust wireless interrogation for sensors and transducers: A non-hermitian telemetry technique," *IEEE Trans. Instrum. Meas.*, vol. 70, pp. 1–9, 2021, doi: 10.1109/TIM.2021.3107057.

[21] L. Zhu, H. Huang, M. M.-C. Cheng, and P.-Y. Chen, "Compact, flexible harmonic transponder sensor with multiplexed sensing capabilities for rapid, contactless microfluidic diagnosis," *IEEE Trans. Microw. Theory Techn.*, vol. 68, no. 11, pp. 4846–4854, Nov. 2020, doi: 10.1109/TMTT.2020.3006286.

[22] L. Zhu, M. Farhat, Y.-C. Chen, K. N. Salama, and P.-Y. Chen, "A compact, passive frequency-hopping harmonic sensor based on a microfluidic reconfigurable dual-band antenna," *IEEE Sensors J.*, vol. 20, no. 21, pp. 12495–12503, Nov. 2020, doi: 10.1109/JSEN.2020.3000778.

[23] M. Hajizadegan et al., "Graphene sensing modulator: Toward low-noise, self-powered wireless microsensors," *IEEE Sensors J.*, vol. 17, no. 22, pp. 7239–7247, Aug. 2017, doi: 10.1109/JSEN.2017.2737699.

[24] L. Zhu, N. Alsaab, M. M.-C. Cheng, and P.-Y. Chen, "A zero-power ubiquitous wireless liquid-level sensor based on microfluidic-integrated microstrip antenna," *IEEE J. Radio Freq. Identificat.*, vol. 4, no. 3, pp. 265–274, Sep. 2020, doi: 10.1109/JRFID.2020.3004351.

[25] A. Somov, A. Baranov, A. Savkin, D. Spirjakin, A. Spirjakin, and R. Passerone, "Development of wireless sensor network for combustible gas monitoring," *Sens. Actuators A, Phys.*, vol. 171, no. 2, pp. 398–405, Nov. 2011.

[26] M. A. Matin and M. Islam, "Overview of wireless sensor network," in *Wireless Sensor Networks-Technology Protocols*. New York, NY, USA: Artech House, 2012, pp. 1–3.

[27] F. Tlili, N. Hamdi, and A. Belghith, "Accurate 3D localization scheme based on active RFID tags for indoor environment," in *Proc. IEEE Int. Conf. RFID-Technolog. Appl. (RFID-TA)*, Nov. 2012, pp. 378–382.

[28] H. Huang, M. Sakhdari, M. Hajizadegan, A. Shahini, D. Akinwande, and P.-Y. Chen, "Toward transparent and self-activated graphene harmonic transponder sensors," *Appl. Phys. Lett.*, vol. 108, no. 17, Apr. 2016, Art. no. 173503, doi: 10.1063/1.4948254.

[29] L. Zhu, N. Alkhaldi, H. M. Kadry, S. Liao, and P. Y. Chen, "A compact hybrid-fed microstrip antenna for harmonics-based radar and sensor systems," *IEEE Antennas Wireless Propag. Lett.*, vol. 17, pp. 2444–2448, 2018.

[30] H. Huang, P.-Y. Chen, C.-H. Hung, R. Gharpurey, and D. Akinwande, "Frequency hopped wireless passive sensing system with harmonic transponder antenna sensor," in *IEEE MTT-S Int. Microw. Symp. Dig.*, May 2015, pp. 1–4.

[31] V. Viikari, H. Seppa, T. Mattila, and A. Alastalo, "Wireless ferroelectric resonating sensor," *IEEE Trans. Ultrason., Ferroelectr., Freq. Control*, vol. 57, no. 4, pp. 785–791, Apr. 2010.

[32] V. Viikari, H. Seppa, and D.-W. Kim, "Intermodulation read-out principle for passive wireless sensors," *IEEE Trans. Microw. Theory Techn.*, vol. 59, no. 4, pp. 1025–1031, Apr. 2011.

[33] M. M. Islam, K. Rasilainen, and V. Viikari, "Implementation of sensor RFID: Carrying sensor information in the modulation frequency," *IEEE Trans. Microw. Theory Techn.*, vol. 63, no. 8, pp. 2672–2681, Aug. 2015, doi: 10.1109/TMTT.2015.2446476.

[34] H. C. Gomes and N. B. Carvalho, "The use of intermodulation distortion for the design of passive RFID," in *Proc. Eur. Radar Conf.*, Oct. 2007, pp. 377–380, doi: 10.1109/EURAD.2007.4405016.

[35] F. Schedin et al., "Detection of individual gas molecules adsorbed on graphene," *Nature Mater.*, vol. 6, pp. 652–655, Jul. 2007, doi: 10.1038/nmat1967.

[36] N. Mohanty and V. Berry, "Graphene-based single-bacterium resolution biodevice and DNA Transistor: Interfacing graphene derivatives with nanoscale and microscale biocomponents," *Nano Lett.*, vol. 8, no. 12, pp. 4469–4476, 2008, doi: 10.1021/nl802412n.

[37] R. S. Sundaram, C. Gómez-Navarro, K. Balasubramanian, M. Burghard, and K. Kern, "Electrochemical modification of graphene," *Adv. Mater.*, vol. 20, no. 16, pp. 3050–3053, Aug. 2008, doi: 10.1002/adma.200800198.

[38] L. Zhu, M. Farhat, K. N. Salama, and P.-Y. Chen, "Two-dimensional materials-based radio frequency wireless communication and sensing systems for Internet-of-Things applications," in *Emerging 2D Materials and Devices for the Internet of Things*. Amsterdam, The Netherlands: Elsevier, 2020, pp. 29–57, doi: 10.1016/B978-0-12-818386-1.00002-3.

[39] R. Pearce, T. Iakimov, M. Andersson, L. Hultman, A. L. Spetz, and R. Yakimova, "Epitaxially grown graphene based gas sensors for ultra sensitive NO_2 detection," *Sens. Actuators B, Chem.*, vol. 155, no. 2, pp. 451–455, Jul. 2011.

[40] O. V. Kotov, M. A. Kol'chenko, and Y. E. Lozovik, "Ultrahigh refractive index sensitivity of TE-polarized electromagnetic waves in graphene at the interface between two dielectric media," *Opt. Exp.*, vol. 21, no. 11, pp. 13533–13546, 2013.

[41] H. Pinto and A. Markevich, "Electronic and electrochemical doping of graphene by surface adsorbates," *Beilstein J. Nanotechnol.*, vol. 5, pp. 1842–1848, Oct. 2014.

[42] X. Tan et al., "Ultrasensitive and selective bacteria sensors based on functionalized graphene transistors," *IEEE Sensors J.*, vol. 22, no. 6, pp. 5514–5520, Mar. 2022, doi: 10.1109/JSEN.2022.3147229.

[43] Y. Ohno, K. Maehashi, Y. Yamashiro, and K. Matsumoto, "Electrolyte-gated graphene field-effect transistors for detecting pH and protein adsorption," *Nano Lett.*, vol. 9, no. 9, pp. 3318–3322, Sep. 2009.

[44] H. J. Yoon, D. H. Jun, J. H. Yang, Z. X. Zhou, S. S. Yang, and M. M.-C. Cheng, "Carbon dioxide gas sensor using a graphene sheet," *Sens. Actuator B, Chem.*, vol. 157, no. 1, pp. 310–313, Sep. 2011.

[45] P. Alonso-Cristobal et al., "Highly sensitive DNA sensor based on upconversion nanoparticles and graphene oxide," *ACS. Appl. Mater. Interfaces*, vol. 7, no. 23, pp. 12422–12429, 2015.

[46] Y. Ohno, K. Maehashi, and K. Matsumoto, "Label-free biosensors based on aptamer-modified graphene field-effect transistors," *J. Amer. Chem. Soc.*, vol. 132, pp. 18012–18013, Dec. 2010.

[47] L. Xiang, Z. Wang, Z. Liu, S. E. Weigum, Q. Yu, and M. Y. Chen, "Inkjet-printed flexible biosensor based on graphene field effect transistor," *IEEE Sensors J.*, vol. 16, no. 23, pp. 8359–8364, Dec. 2016.

[48] P.-Y. Chen and A. Alu, "Atomically thin surface cloak using graphene monolayers," *ACS Nano*, vol. 5, no. 7, pp. 5855–5863, Jul. 2011, doi: 10.1021/nn201622e.

[49] P.-Y. Chen and A. Alu, "Terahertz metamaterial devices based on graphene nanostructures," *IEEE Trans. THz Sci. Technol.*, vol. 3, no. 6, pp. 748–756, Nov. 2013, doi: 10.1109/TTHZ.2013.2285629.

[50] P. Y. Chen, C. Argyropoulos, and A. Alù, "Terahertz antenna phase shifters using integrally-gated graphene transmission-lines," *IEEE Trans. Antennas Propag.*, vol. 61, no. 4, pp. 1528–1537, Apr. 2013, doi: 10.1109/TAP.2012.2220327.

[51] M. Orlita et al., "Approaching the dirac point in high-mobility multilayer epitaxial graphene," *Phys. Rev. Lett.*, vol. 101, no. 26, Dec. 2008, Art. no. 267601.

[52] S. M. Sze, Y. Li, and K. K. Ng, *Physics of Semiconductor Devices*. Hoboken, NJ, USA: Wiley, 2021.

[53] V. E. Dorgan, M.-H. Bae, and E. Pop, "Mobility and saturation velocity in graphene on SiO_2," *Appl. Phys. Lett.*, vol. 97, no. 8, Aug. 2010, Art. no. 082112, doi: 10.1063/1.3483130.

[54] A. Pacheco-Sanchez, J. N. Ramos-Silva, E. Ramirez-Garcia, and D. Jimenez, "A small-signal GFET equivalent circuit considering an explicit contribution of contact resistances," *IEEE Microw. Wireless Compon. Lett.*, vol. 31, no. 1, pp. 29–32, Jan. 2021, doi: 10.1109/LMWC.2020.3036845.

[55] K. N. Parrish, M. E. Ramón, S. K. Banerjee, and D. Akinwande, "A compact model for graphene FETs for linear and non-linear circuits," in *Proc. Int. Conf. Simulation Semiconductor Processes Devices*, Denver, CO, USA, 2012, pp. 75–78.

[56] H. Huang et al., "Chemical-sensitive graphene modulator with a memory effect for Internet-of-Things applications," *Microsyst. Nanoeng.*, vol. 2, no. 1, Dec. 2016, Art. no. 16018, doi: 10.1038/micronano.2016.18.

[57] M. Hajizadegan, M. Sakhdari, S. Abbasi, and P.-Y. Chen, "Machine learning assisted multi-functional graphene-based harmonic sensors," *IEEE Sensors J.*, vol. 21, no. 6, pp. 8333–8340, Mar. 2021, doi: 10.1109/JSEN.2020.3046455.

[58] K. N. Parrish and D. Akinwande, "An exactly solvable model for the graphene transistor in the quantum capacitance limit," *Appl. Phys. Lett.*, vol. 101, no. 5, Jul. 2012, Art. no. 053501.

[59] J. Tian, A. Katsounaros, D. Smith, and Y. Hao, "Graphene field-effect transistor model with improved carrier mobility analysis," *IEEE Trans. Electron Devices*, vol. 62, no. 10, pp. 3433–3440, Oct. 2015.

[60] G. M. Landauer, D. Jímenez, and J. L. González, "An accurate and Verilog-A compatible compact model for graphene field-effect transistors," *IEEE Trans. Nanotechnol.*, vol. 13, no. 5, pp. 895–904, Sep. 2014.

[61] S. Wang, P. K. Ang, Z. Wang, A. L. L. Tang, J. T. L. Thong, and K. P. Loh, "High mobility, printable, and solution-processed graphene electronics," *Nano Lett.*, vol. 10, no. 1, pp. 92–98, Jan. 2010.

[62] D. Svintsov, V. Ryzhii, A. Satou, T. Otsuji, and V. Vyurkov, "Carrier-carrier scattering and negative dynamic conductivity in pumped graphene," *Opt. Exp.*, vol. 22, no. 17, Aug. 2014, Art. no. 19873, doi: 10.1364/OE.22.019873.

[63] W. Zhu, V. Perebeinos, M. Freitag, and P. Avouris, "Carrier scattering, mobilities, and electrostatic potential in monolayer, bilayer, and trilayer graphene," *Phys. Rev. B, Condens. Matter*, vol. 80, no. 23, Dec. 2009, Art. no. 235402.

[64] J. Martin et al., "Observation of electron-hole puddles in graphene using a scanning single-electron transistor," *Nature Phys.*, vol. 4, no. 2, pp. 144–148, 2008.

[65] S. A. Thiele, J. A. Schaefer, and F. Schwierz, "Modeling of graphene metal-oxide-semiconductor field-effect transistors with gapless large-area graphene channels," *J. Appl. Phys.*, vol. 107, no. 9, May 2010, Art. no. 094505, doi: 10.1063/1.3357398.

[66] D. Jimenez and O. Moldovan, "Explicit drain-current model of graphene field-effect transistors targeting analog and radio-frequency applications," *IEEE Trans. Electron Devices*, vol. 58, no. 11, pp. 4049–4052, Nov. 2011, doi: 10.1109/TED.2011.2163517.

Minye Yang received the bachelor's degree in optical and electronic information from the Huazhong University of Science and Technology, Hubei, China, in 2014, and the M.Sc. degree in electrical and computer engineering from Wayne State University, Detroit, MI, USA, in 2019. He is currently pursuing the Ph.D. degree in electrical and computer engineering with the University of Illinois at Chicago, Chicago, IL, USA.

His research interests include applied electromagnetics, radio frequency (RF), microwave antennas and circuits, metasurfaces, wireless sensors, and integrated systems.

Zhilu Ye received the B.S. degree in microelectronics from the Huazhong University of Science and Technology, Wuhan, China, in 2018, and the master's degree in electrical engineering from Arizona State University, Tempe, AZ, USA, in 2019. She is pursuing the Ph.D. degree with the University of Illinois at Chicago, Chicago, IL, USA.

Her research interests include radio frequency (RF) and microwave sensors, wireless communication, and wearable electronics.

Chia-Heng Sun received the M.S. degree in physics from National Central University, Taoyuan, Taiwan, in 2015. He is currently pursuing the Ph.D. degree in electrical and computer engineering with the University of Illinois at Chicago, Chicago, IL, USA.

His research interests include measurement and fabrication of 2-D materials and nanodevices.

Liang Zhu received the M.Sc. degree in optics from Sun Yat-sen University, Guangzhou, China, in 2015, and the Ph.D. degree in electrical and electronics engineering from the University of Illinois at Chicago, Chicago, IL, USA, in 2021.

He is currently an Antenna Engineer with Maxtena, Inc., Rockville, MD, USA. His research interests include RF/microwave antennas and circuits, energy harvesting platforms, and wireless sensors.

Mehdi Hajizadegan (Senior Member, IEEE) received the M.Sc. degree from Tarbiat Modares University, Tehran, Iran, in 2013, and the Ph.D. degree in electrical engineering from the University of Illinois at Chicago, Chicago, IL, USA, in 2020.

He was a Research Assistant with Wayne State University, Detroit, MI, USA, the University of Illinois at Chicago, and the National Science Foundation I-Corps Program, from 2015 to 2020. His research interests include graphene and other carbon-based biosensors, parity time (PT)-symmetry-based wearable biosensors and leaky wave antennas, and passive and active electromagnetic metamaterials and plasmonics and their applications for energy harvesting.

Pai-Yen Chen (Senior Member, IEEE) received the B.S. and M.S. degrees from National Chiao Tung University, Hsinchu, Taiwan, in 2004 and 2006, respectively, and the Ph.D. degree from the University of Texas at Austin, Austin, TX, USA, in 2013.

He was the Research Scientist with the Intellectual Ventures' Metamaterial Commercialization Center, Bellevue, WA, USA, from 2013 to 2014, and a Research Staff with the National Nano Device Laboratory, Hsinchu, from 2006 to 2009. He is an Associate Professor with the Department of Electrical and Computer Engineering, University of Illinois at Chicago, Chicago, IL, USA. He has been involved in multidisciplinary research on applied electromagnetics, radio frequency (RF)/microwave antennas and circuits, wireless micro-/nanosensors and integrated systems, as well as nanoelectromagnetism in plasmonics and nanophotonics.

Dr. Chen has received quite a few prestigious awards, including the National Science Foundation (NSF) CAREER Award, the IEEE Sensors Council Young Professional Award, the IEEE Raj Mittra Travel Grant (RMTG) Award, the Society of Photo-Optical Instrumentation Engineers (SPIE) Rising Researcher Award, the Applied Computational Electromagnetics Society (ACES) Early Career Award, the PhotonIcs and Electromagnetics Research Symposium (PIERS) Young Professional Award, the Institute of Physics (IOP) Measurement Science and Technology Emerging Leader, the Young Scientist Awards from Union Radio-Scientifique Internationale (URSI) General Assembly and URSI Commission B: Electromagnetics, the Air Force Research Laboratory Faculty Fellowship, the National Argonne Laboratory Director's Fellowship, the College of Engineering Faculty Research Excellence Award, the Donald Harrington Fellowship, the Taiwan Ministry of Education Study Abroad Award, and the United Microelectronics Corporation Scholarship; and quite a few student paper awards and travel grants from major IEEE conferences (as a student or with advised students), including the U.S National Committee-URSI (USNC-URSI) Ernest K. Smith Student Paper Award in 2012, the IEEE Antennas and Propagation Symposium in 2011, 2013, 2016, and 2021, the IEEE Sensors Conferences in 2016, the IEEE International Microwave Symposium in 2015, and the IEEE Wireless Power Transfer Conference in 2021. He is on the Board of Directors of ACES for the period 2021–2024. He also serves as an Associate Editor for IEEE SENSORS JOURNAL, IEEE TRANSACTIONS ON ANTENNAS AND PROPAGATION, IEEE JOURNAL OF RADIO FREQUENCY IDENTIFICATION (IEEE JRFID), and IEEE JOURNAL OF ELECTROMAGNETICS, RF AND MICROWAVES IN MEDICINE AND BIOLOGY (IEEE-JERM), and a Guest Editor for several international journals. He was a former Associate Editor of *Applied Electromagnetics*.